

# Mechanism of DSA effect correlating to the macroscopic PLC banding in high-Mn austenitic steel

Sukyoung Hwang <sup>a,\*</sup>, Myeong-Heom Park <sup>a,\*</sup>, Yu Bai <sup>b</sup>, Avala Lavakumar <sup>a, c</sup>, Akinobu Shibata

<sup>a, d, e</sup>, Hiroki Adachi <sup>f</sup>, Masugu Sato <sup>g</sup>, Nobuhiro Tsuji <sup>a, c\*</sup>

<sup>a</sup> *Department of Materials Science and Engineering, Kyoto University, Yoshida-honmachi,  
Sakyo-ku, Kyoto 606-8501, Japan*

<sup>b</sup> *School of Materials Science and Engineering, Dalian university of Technology, 2 Linggong  
Road, Dalian City, Liaoning Province 116024, P.R. China*

<sup>c</sup> *Department of Metallurgy and Material Engineering, Indian Institute of Technology Ropar,  
Punjab 140 001, India*

<sup>d</sup> *Elements Strategy Initiative for Structural Materials (ESISM), Kyoto University, Yoshida-  
honmachi, Sakyo-ku, Kyoto 606-8501, Japan*

<sup>e</sup> *National Institute for Materials Science (NIMS), 1-2-1 Sengen, Tsukuba 305-0047, Japan*

<sup>f</sup> *Department of Materials and Synchrotron Radiation Engineering, Graduate School of  
Engineering, University of Hyogo, Himeji 671-2280, Japan*

<sup>g</sup> *Japan Synchrotron Radiation Research Institute (JARI), Sayo-gun, Hyogo 679-5198,  
Japan*

\*Corresponding authors: Nobuhiro Tsuji ([nobuhiro-tsuji@mtl.kyoto-u.ac.jp](mailto:nobuhiro-tsuji@mtl.kyoto-u.ac.jp)), Sukeyoung Hwang ([hwang.sukeyoung.8p@kyoto-u.ac.jp](mailto:hwang.sukeyoung.8p@kyoto-u.ac.jp)), Myeong-Heom Park ([park.myeongheom.8r@kyoto-u.ac.jp](mailto:park.myeongheom.8r@kyoto-u.ac.jp))

## Abstract

Mechanism of dynamic strain aging (DSA) effect in high-Mn austenitic steel, and its correlation with the Portevin-Le Chatelier (PLC) banding, was elucidated using the *in-situ* synchrotron XRD measurement and digital image correlation (DIC) method during tensile test. The average dislocation velocity beyond the PLC band ranged from  $10^{-2}$  to  $10^{-1}$  nm/s, while reached to the order of  $10^0$  nm/s within the PLC band. In comparison, carbon diffusivity was significantly lower, allowing carbon atoms to diffuse only from  $10^{-7}$  to  $10^{-9}$  nm in one second. The findings indicate that dislocations beyond the advancing PLC band were pinned by nearby carbon atoms, while dislocations within the PLC band became de-pinned from the carbons. Such localized pinning and de-pinning of dislocations occurred sequentially during deformation, appearing as the propagation of PLC bands in macroscopic scale.

**Keywords:** Portevin–Le Chatelier (PLC) band; dynamic strain aging (DSA); digital image correlation (DIC); *in-situ* synchrotron XRD; Average dislocation velocity

The dynamic strain aging (DSA) effect in steel has been considered as the result of dynamic interaction between dislocations and carbon atoms during deformation [1–3]. According to the conventional theory of the DSA effect, carbon atoms are considered to diffuse to catch up with mobile dislocations under specific deformation conditions, such as intermediate temperatures [4–6] or slow strain rates [4–9], where they then pin the mobile dislocations, creating the Cottrell atmosphere. The concept was extended to high-Mn austenitic steels, by many researchers substituting partial dislocations for perfect dislocation in their explanations of the DSA effect [10–13]. Lee et al. [12] and De Cooman et al. [10] proposed that the DSA effect originated from the interaction between the leading partial dislocation and the Mn-C pair. As a leading partial dislocation glides on the {111} plane, a nearby carbon atom is forcibly transferred from an octahedral site to an unstable tetrahedral site. Subsequently, the carbon atom reorients itself by a single diffusive hop to an octahedral site adjacent to a Mn atom, increasingly forming Mn-C pairs. They argued that these Mn-C pairs acted as obstacles for dislocation glide and enhanced the DSA effect. In contrast, Oh et al. [13] contended that the DSA effect arose from carbon diffusion along the dislocation line, so-called dislocation pipe diffusion. According to their explanation, a mobile dislocation is arrested by immobile dislocation, during which carbon atoms can diffuse from the immobile dislocation to the mobile dislocation. Subsequently, the carbon atoms diffuse again along the dislocation line, leading to the pinning of the mobile dislocation. They contended that higher

1 carbon content observed along the dislocation line in atom probe tomography (APT) resulted  
2  
3  
4  
5 from the dislocation pipe diffusion of carbons. In both the case of Mn-C couples and the pipe  
6  
7  
8 diffusion of carbon, carbon plays a key role in the DSA effect. However, it would be natural  
9  
10  
11 for carbon atoms to segregate along the nearby dislocation if enough time was allowed after  
12  
13  
14 unloading the tensile specimen. To develop a deeper understanding of the nature of dynamic  
15  
16  
17 strain ageing during deformation, it is essential to evaluate the real-time interaction between  
18  
19  
20  
21 dislocations and carbons during a tensile test.  
22  
23

24 In earlier research, it has been clarified that serration behavior on the global stress-  
25  
26  
27 strain curve in high-Mn austenitic steel perfectly corresponded to local heterogeneous  
28  
29  
30 deformation characterized by the formation, propagation and annihilation of so-called  
31  
32  
33 Portevin–Le Chatelier (PLC) bands, i.e., PLC banding [4,14–16]. However, ever since Kubin  
34  
35  
36 and Estrin [17] established foundational work several decades ago on predicting dislocation de-  
37  
38  
39 pinning in the propagating PLC band and subsequent re-pinning of dislocations based on a  
40  
41  
42 mathematical model, their predictions have yet to be experimentally proven.  
43  
44  
45

46 In the present study, we aim to reveal the mechanism of DSA in correlation with  
47  
48  
49 macroscopic local deformation behavior, i.e., PLC banding. We investigated the average  
50  
51  
52 dislocation velocity concerning the local PLC banding by simultaneously applying *in-situ*  
53  
54  
55 synchrotron XRD measurement and digital image correlation (DIC) method during the tensile  
56  
57  
58 test. Additionally, carbon diffusivity was estimated in comparison with the dislocation  
59  
60  
61

velocity to understand the nature of DSA effect in high-Mn austenitic steel.

A high-Mn austenitic steel having an average chemical composition of Fe-22Mn-0.6C (wt. %) was used in this study. The hot-forged plate, originally 12 mm thick, underwent four cycles of cold-rolling and annealing treatments [14,18,19]. SEM-BSE image of the specimen, annealed at 800 °C for 0.3 ks and then water-quenched in the final annealing step, is shown in **Figure 1**. The specimen had a fully recrystallized microstructure, and exhibited a mean grain size of 2.0 μm, including annealing twin boundaries.

To evaluate the change in the average dislocation velocity concerning local PLC banding, *in-situ* synchrotron XRD measurement and DIC method were simultaneously performed during tensile test. The experiment was carried out at the high energy (HE) synchrotron beam line of BL46 XU at SPring-8 of JASRI. The configuration of the synchronized DIC method and *in-situ* synchrotron XRD measurement during the tensile test is shown in the supplementary material (**Fig. S1**). After a precise setup, the tensile test was conducted at an initial strain rate of  $8.3 \times 10^{-4} \text{ s}^{-1}$  at room temperature. For the discussion of carbon diffusivity, the change in local temperature was estimated using a thermography camera (FLIR, CPA-E75S). The temperature distribution of the tensile specimen was recorded at 30 FPS (frame per second) and quantitatively analyzed by using FLIRTools software.

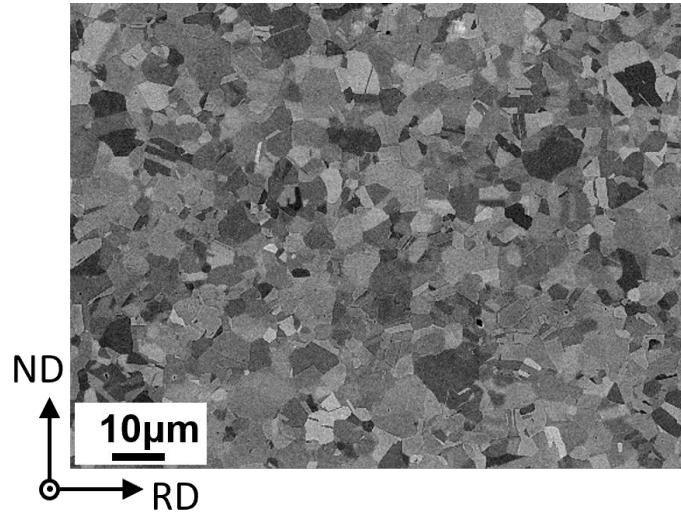


**Fig. 1** SEM-BSE image of the 22Mn-0.6C steel with a mean grain size of 2.0  $\mu\text{m}$ , observed from the transverse direction (TD) of the rolled sheet.

The synchrotron XRD measurement and DIC analysis during the tensile test were synchronized precisely, and the results are shown in **Fig. 2**. In **Fig. 2 (a)**, the changes in local stress (red) and dislocation density (blue) at the XRD beam position, as well as the global true stress curve (black), are plotted as a function of true strain. The local stress referred to the local principal stress at the XRD beam position ( $\sigma_1$ , parallel to the tensile direction (TD), which was converted from the stress applied on the (200) plane ( $\sigma_{200}$ ) forming Bragg's angle relative to the TD). The conversion from  $\sigma_{200}$  to  $\sigma_1$  utilized Mohr's circle for the uniaxial tensile test, and the detailed calculation is presented in the supplementary material (**Fig. S2**). Dislocation density was determined from changes in the full width half-maximums (FWHMs) of diffraction peaks during the tensile test using the Williamson-Hall method [20]. It was assumed that most of the peak broadening, particularly in the regions above the bottom part of

the diffraction peaks, was caused by accumulated dislocations [14], acknowledging that the bottom part may also broaden due to stacking faults [21,22]. Our previous work showed that deformation twins formed significantly in carbon-free high-Mn steel without exhibiting serration behavior [23]. In contrast, it was reported by Luo and Huang [24] that carbon-containing high-Mn steels exhibited serration behavior in higher temperature regions where deformation twinning was barely activated. This suggests that the interaction between dislocations and carbons, rather than deformation twinning (or its interaction with carbons), is the dominant factor contributing to the serration behavior. Accordingly, we focused our discussion on dislocation behavior in relation to the correlation between PLC banding and the DSA effect. Both the local stress and global true stress increased with deformation, and serration behavior was also observed on the stress-strain curves. Dislocation density increased in a stepwise manner during deformation, remaining relatively flat during most of the deformation periods but significantly increasing at certain strains. For a more detailed investigation, the graph during a late stage of deformation is enlarged in [Fig. 2 \(b\)](#). Thin broken lines on the global true stress-strain curve indicate the true strain at each serration peak. The serration peaks on the global true stress-strain curve perfectly coincided with the peaks of the local stress at the XRD beam position, indicating that the entire tensile specimen, including the XRD beam position, experienced the sudden increase in stress, forming the serration peak. The numbers (1) to (5) on the dislocation density ([Fig. 2 \(b\)](#)) curve correspond to the strain-

rate maps (1) to (5) in **Fig. 2 (c)**, during which a PLC band (red colored region with a higher strain rate) was propagating near the XRD beam position. Comparing **Fig. 2 (b)** and **Fig. 2 (c)**, when the PLC band was away from the beam position ((1) in **Fig. 2 (c)**), there was no increase in dislocation density (point (1) in **Fig. 2 (b)**). At (2) in **Fig. 2 (c)**, as the PLC band was about to enter the beam position, dislocation density started to increase drastically (point (2) in **Fig. 2 (b)**). At (3) in **Fig. 2 (c)**, as the PLC band was propagating over the beam position, the dislocation density was increasing significantly (point (3) in **Fig. 2 (b)**). At (4) in **Fig. 2 (c)**, as the PLC band was leaving the beam position, the dislocation density stopped increasing and turned into a flat curve. At (5) in **Fig. 2 (c)**, once the PLC band completely left the beam position, the increase in dislocation density became very small again (point (5) in **Fig. 2 (b)**). It was conclusively observed that the sudden increase in the dislocation density (point (2) to (4) in **Fig. 2 (b)**) perfectly corresponded to the passage of the PLC band through the beam position ((2) to (4) in **Fig. 2 (c)**). Furthermore, as shown in **Fig. 2 (b)**, it was noteworthy that the local stress at the beam position increased drastically by  $\Delta\sigma$  during the passage of the PLC band on the beam position.



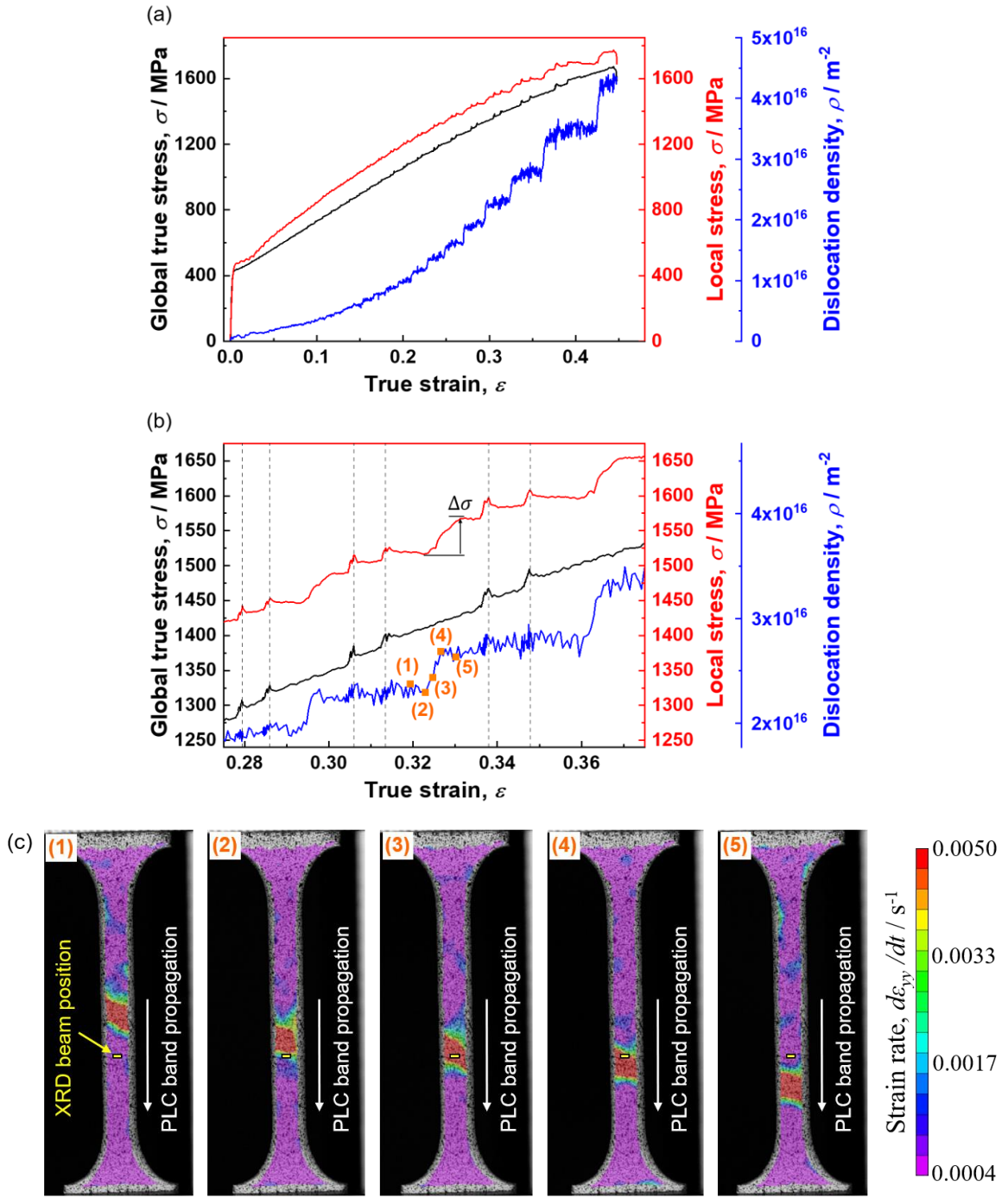


**Fig. 2** (a) The changes of global true stress (black, left y-axis), local stress at the XRD beam position (red, the first right-axis), and dislocation density (blue, the second right y-axis) are shown as a function of true strain. (b) Curves in the true strain range from 0.275 to 0.375, enlarged from (a). Serration peaks are indicated by thin broken lines. The local stress increment ( $\Delta\sigma$ ) is indicated by an arrow on the local stress curve. The points (1) to (5) marked on the dislocation density curve correspond to the DIC images of (1) to (5) in (c). (c) DIC strain-rate maps corresponding to the propagation of the PLC band near the XRD beam position. The yellow point in each DIC image indicates the XRD beam position.

Through the synchronized XRD measurement and DIC analysis, it was possible to simultaneously obtain both the local dislocation density and local strain at the beam position.

According to Orowan et al. [25], macroscopic shear deformation is produced by mobile dislocation density and the average distance that the dislocations glide, as:

$$\gamma = \rho b \bar{x} \quad (1)$$

Here,  $\gamma$  is the shear strain,  $\rho$  is the mobile dislocation density,  $b$  is the magnitude of Burger vector (0.2552 nm for the current material), and  $\bar{x}$  is the average distance of dislocation glide.

In the present study, the local strain obtained from the DIC analysis was local tensile strain.

Therefore, the local tensile strain was converted into local shear strain ( $\gamma$ ) for calculating the average distance of dislocation glide ( $\bar{x}$ ) at the XRD beam position. The conversion process

from tensile strain to shear strain is described in the supplementary material. A total of 128

sets of local shear strain ( $\gamma$ ) and local dislocation density ( $\rho$ ) were investigated after a global

true strain of 0.1, due to the weak serration behavior observed in the early stage of deformation

(Fig. 2 (a)). The average distance of dislocation glide ( $\bar{x}$ ) at the XRD beam position,

calculated using Equation (1), is plotted against the global true strain in Fig. 3 (a). The

average distance of dislocation glide ( $\bar{x}$ ) at the XRD beam position will henceforth be termed

‘dislocation glide distance’. In this study, the dislocation glide distance was calculated for two

distinct groups relative to the PLC band position: one group within the PLC band (red dots),

and the other beyond the PLC band (blue dots). For example, in **Fig. 2 (c)**, the periods at maps (2), (3), and (4) are indicated by red dots, while the periods at maps (1) and (5) are indicated by blue dots. Overall, the dislocation glide distance decreased as the deformation progressed, probably due to increased dislocation-dislocation interactions. Interestingly, upon the PLC band enters the XRD beam position, corresponding to the transition period from blue to red dots, a sharp increase in the dislocation glide distance was observed.

For a detailed investigation, dislocation velocity was investigated by modifying Eq. (1) as follows:

$$\dot{\gamma} = \frac{d\gamma}{dt} = \rho b \frac{d\bar{x}}{dt} = \rho b \bar{v}_d \quad (2)$$

Here,  $\dot{\gamma}$  is the shear strain rate,  $t$  is the time, and  $\bar{v}_d$  is the average dislocation velocity.

The calculated average dislocation velocity is plotted as a function of true strain in **Fig. 3 (b)**.

Similarly, as with the dislocation glide distance (**Fig. 3 (a)**), the average dislocation velocity

within the PLC band is colored red, and that beyond the PLC band is colored blue. The term

‘average dislocation velocity’ will hereafter be shortened to ‘dislocation velocity’. The

dislocation velocity remained consistently below  $1.5 \times 10$  nm/s, irrespective of the position of

the PLC band. It was also notable that the dislocation velocity within the PLC band (red)

decreased as the true strain increased. Interestingly, the dislocation velocity within the PLC

band (red) repeatedly formed sharp peaks, reaching over  $10^1$  nm/s, while that beyond the PLC

band (blue) remained as slow as  $10^{-2}$  to  $10^{-1}$  nm/s. That is, the dislocation velocity within the

PLC band was 100 to 1000 times faster than that beyond the PLC band. Such differences in the dislocation glide distance (**Fig. 3 (a)**) and dislocation velocity (**Fig. 3 (b)**) in relation to the local PLC banding proved that the dislocations beyond the PLC band were pinned by carbons, whereas the dislocations within the PLC band were de-pinned from carbons.

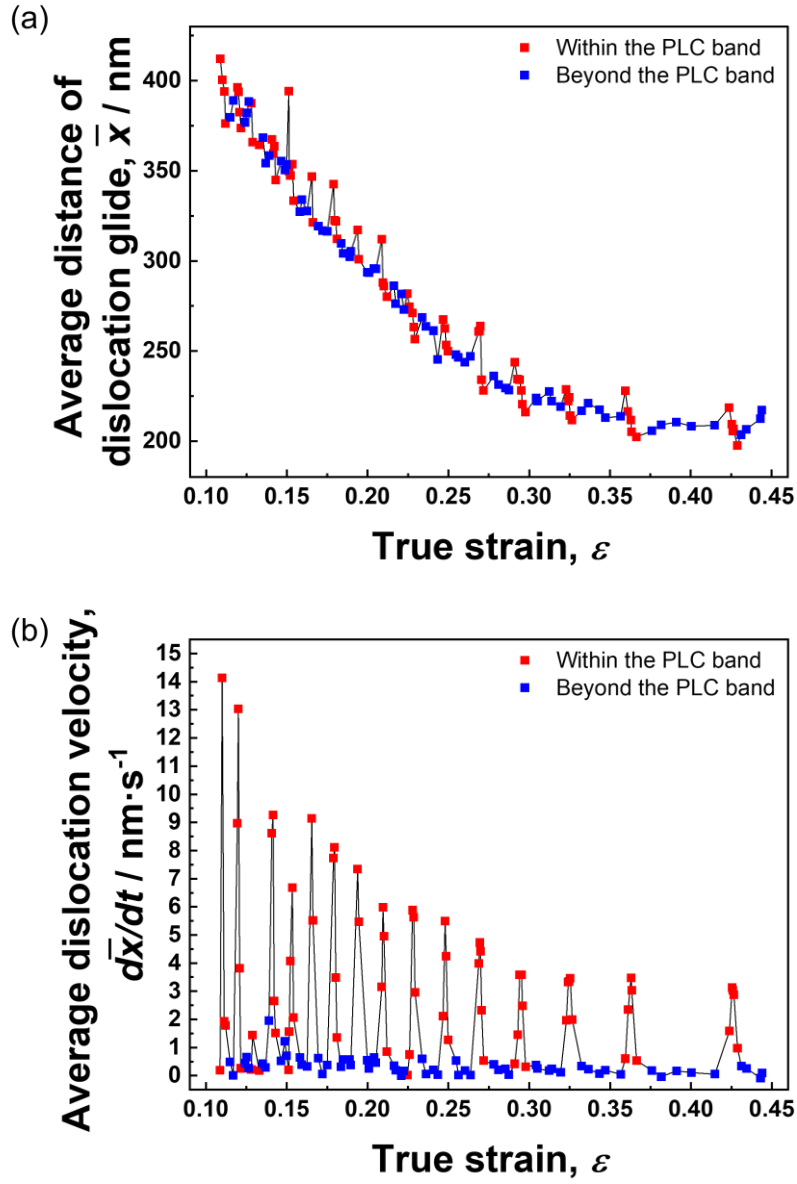


**Fig. 3** Change in (a) average distance of dislocation glide ( $\bar{x}$ ) at the XRD beam position and (b) average dislocation velocity, plotted as a function of true strain. Data points within the PLC band are colored red, and those beyond the PLC band are colored blue.

Next, carbon diffusivity in the present material was investigated in comparison with the dislocation velocity obtained above. The diffusion coefficient of carbon ( $D_c$ ) is expressed

using Arrhenius equation, as follows:

$$D_c = D_0 \exp\left(-\frac{Q}{RT}\right) \quad (3)$$

Here,  $D_0$  is the pre-exponential factor,  $R$  is the gas constant,  $T$  is the temperature, and  $Q$  is the activation energy for carbon diffusion. **Fig. 4 (a)** shows local temperature maps at a late stage of deformation, which corresponded to one cycle of PLC banding. The PLC bands exhibited higher temperature due to strain localization. A PLC band nucleated near the gage center in (1), propagated upward in (2, 3), and annihilated at the upper shoulder part in (4). Subsequently, the PLC band nucleated near the gage center (5), propagated downward in (6, 7), and annihilated at the lower shoulder part in (8). As shown in the inset image in **Fig. 4 (a)**, an analyzed spot was set in the gage part, and the change in local temperature was plotted as a function of experimental time in **Fig. 4 (b)**. The local temperature fluctuated during deformation, and the temperature fluctuation, i.e., the temperature difference before and after the passage of the PLC band, increased as deformation progressed. It was found that the temperature difference within the PLC band and beyond the PLC band was 2.9 °C at the largest. The temperature of the tensile specimen was 20.9 °C before the tensile test, and it increased to 27.1 °C at the point of fracture. Therefore, the temperature ( $T$ ) in Eq. (3) was consistently set to 300 K (27°C), regardless of the position of the PLC band or the stage of the deformation. The  $D_0$  and  $Q$  for the diffusion on interstitial carbon atoms in the austenitic steels [26,27], as well as the calculated  $D_c$  by using Eq. (3), are presented in **Table 1**. The  $D_c$  for the present

material was in the order of  $10^{-12}$  to  $10^{-18}$  nm<sup>2</sup>/s. The diffusion distance of carbon ( $x_c$ ) can be calculated as:

$$x_c = \sqrt{D_c t} \quad (4)$$

Here,  $t$  is the time for carbon diffusion. For example, carbons can diffuse only  $10^{-7}$  to  $10^{-9}$  nm for 1 second. Comparing the carbon diffusivity with the obtained dislocation velocity (**Fig. 3 (b)**), it is difficult to imagine that carbons could diffuse over long distance and effectively interacted with mobile dislocations at 300 K. Curtin et al. [28] predicted the origin of serration behavior in an Al-Mg alloy through simulations demonstrating that a substitutional solute atom (Mg atom) around a dislocation core would spontaneously move a single atomic distance across the slip plane from a compressed region to a tensioned region while awaiting thermal activation, a phenomenon known as cross-core diffusion. According to their simulation results, the cross-core diffusion mechanism is characterized by a lower activation enthalpy of 0.97 eV and a larger driving force of 0.13 eV compared to the lattice diffusion values of 1.20 eV and 0.08 eV respectively, and it showed the best agreement with the experimental results among several proposed models, including pipe diffusion. Meanwhile, Aboufadel et al. [29] observed Mg atoms decorating the dislocation core, with its slip path in the PLC band showing a depletion in solute concentration. Oh et al. [13] reported that the activation enthalpy for serration behavior (or the DSA effect) in high-Mn steel was 0.85 eV, which falls within the broad range of activation enthalpy for pipe diffusion (0.57 to 1.00 eV).

To further clarify the origin of serration behavior in high-Mn steel, a comprehensive evaluation is required that also takes into account interstitial carbon diffusion in the vicinity of the dislocation core. Exploring interstitial carbon diffusion behavior around the dislocation core, which lies beyond scope of continuum model, poses a challenging subject for future study. Nevertheless, our findings along with the results of Curtin et al. [28] and Aboulfadl et al. [29] suggest that lattice diffusion of carbon atoms to the dislocation core is improbable. Instead, dynamic interactions between carbon atoms and dislocations are confined to the vicinity of the dislocation core. Such phenomena occurred beyond the PLC band, where the dislocation velocity became much slower than that within the PLC band (Fig. 3 (b)). However, as the local stress increase in the PLC band (refer to  $\Delta\sigma$  in the Fig. 2 (b)), dislocations started to become de-pinned and glided freely, resulting in the faster dislocation velocity than that observed beyond the PLC band (Fig. 3 (b)). The dislocation density ( $\rho$ ) in this study might be somewhat overestimated because (i) deformation twins were not accounted in the Williamson-Hall method, and (ii) all dislocations were assumed to be mobile. However, the overestimation of dislocation density suggests that the average dislocation velocity in Eq. (2) was actually underestimated at the same shear strain rate. That is, when the dislocation density was overestimated, the difference between carbon diffusivity and dislocation velocity became actually larger, so that long-range diffusion of carbon was less likely to occur. The results obtained in the present study consistently explain that local de-pinning and multiplication of



dislocations occurred repetitively during the tensile deformation, which was observed in a macroscopic scale as the propagation of strain-localized band, i.e., PLC banding.

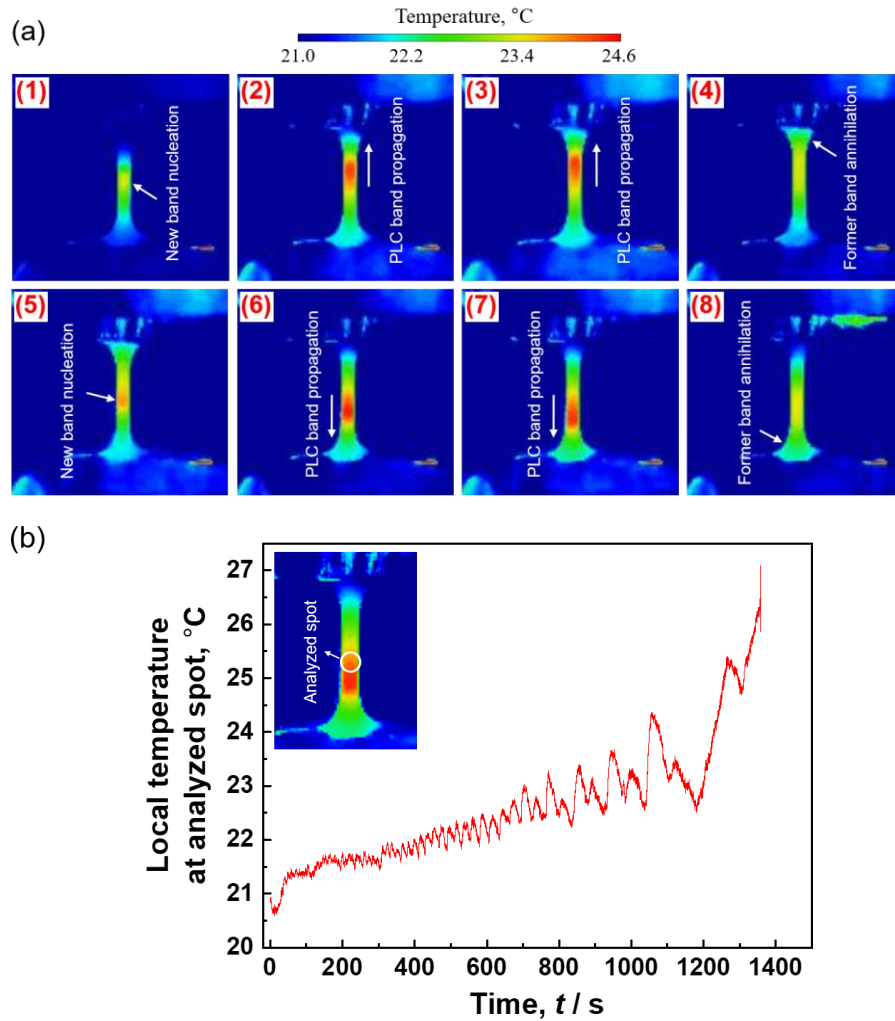


**Fig. 4** (a) Local temperature maps at a late stage of deformation ( $t=1003.9$  s to 1125.4 s), which correspond to one cycle of PLC banding. The magnitude of the local temperature is represented in different colors according to the color bar shown above. PLC bands appear having higher temperature. (b) Changes in the local temperature at an analyzed spot in the gage part till fracture, plotted as a function of experimental time.

**Table 1** (a) Pre-exponential factor ( $D_0$ ) and activation energy ( $Q$ ), as well as the calculated diffusion coefficient ( $D_c$ ) of carbon in austenitic steels.

Material (wt.%)	$D_0$ [ $nm^2/s$ ]	$Q$ [J/mol]	$D_c$ at 300 K [ $nm^2/s$ ]
Fe-15Mn-0.34C [26]	$9 \times 10^{11}$	133800	$4.5 \times 10^{-12}$
SUS304 (0.08%C) [27]	$6.18 \times 10^{14}$	186700	$1.9 \times 10^{-18}$
SUS347 (0.08%C) [27]	$3.5 \times 10^{13}$	168000	$2.0 \times 10^{-16}$
SUS316 (0.08%C) [27]	$1.9 \times 10^{13}$	156500	$1.1 \times 10^{-14}$

## Acknowledgements

The present study was financially supported by JST CREST (JPMJCR1994), Elements Strategy Initiative for Structural Materials (ESISM, No. JPMXP0112101000), and the Grant-in-Aids for Scientific Research (No. 20K14608, 21K20401, 22K18888, 23H00234, 23K13563 and 23K20037), all through the Ministry of Education, Culture, Sports, Science and Technology (MEXT), Japan. The synchrotron radiation experiments (beam-time No. 2018B1760) at Super Photon ring-8 GeV (SPring-8) were performed with the approval of the Japan Synchrotron Radiation Research Institute (JASRI). All the supports are gratefully appreciated.

1  
2  
3  
4  
5  
6  
7  
8  
9  
10  
11  
12  
13  
14  
15  
16  
17  
18  
19  
20  
21  
22  
23  
24  
25  
26  
27  
28  
29  
30  
31  
32  
33  
34  
35  
36  
37  
38  
39  
40  
41  
42  
43  
44  
45  
46  
47  
48  
49  
50  
51  
52  
53  
54  
55  
56  
57  
58  
59  
60  
61  
62  
63  
64  
65

## References

- [1] D. Caillard, Dynamic strain ageing in iron alloys: The shielding effect of carbon, *Acta Mater.* (2016). doi:10.1016/j.actamat.2016.04.018.
- [2] A. van den Beukel, Theory of the effect of dynamic strain aging on mechanical properties, *Phys. Status Solidi.* (1975). doi:10.1002/pssa.2210300120.
- [3] A.H. Cottrell, LXXXVI. A note on the Portevin-Le Chatelier effect, London, Edinburgh, Dublin Philos. Mag. J. Sci. (1953). doi:10.1080/14786440808520347.
- [4] K. Renard, S. Ryelandt, P.J. Jacques, Characterisation of the Portevin-Le Châtelier effect affecting an austenitic TWIP steel based on digital image correlation, *Mater. Sci. Eng. A.* (2010). doi:10.1016/j.msea.2010.01.037.
- [5] A. Saeed-Akbari, A.K. Mishra, J. Mayer, W. Bleck, Characterization and prediction of flow behavior in high-manganese twinning induced plasticity steels: Part II. jerky flow and instantaneous strain rate, *Metall. Mater. Trans. A Phys. Metall. Mater. Sci.* (2012). doi:10.1007/s11661-011-1070-8.
- [6] M. Koyama, E. Akiyama, K. Tsuzaki, Factors Affecting Static Strain Aging Under Stress at Room Temperature in a Fe-Mn-C Twinning-Induced Plasticity Steel, *Tetsu-to-Hagane.* (2014). doi:10.2355/tetsutohagane.100.1123.
- [7] X. Bian, F. Yuan, X. Wu, Correlation between strain rate sensitivity and characteristics of Portevin-LeChâtelier bands in a twinning-induced plasticity steel, *Mater. Sci. Eng. A.*

- (2017). doi:10.1016/j.msea.2017.04.078.
- [8] S.Y. Lee, S.I. Lee, B. Hwang, Effect of strain rate on tensile and serration behaviors of an austenitic Fe-22Mn-0.7C twinning-induced plasticity steel, *Mater. Sci. Eng. A.* (2018). doi:10.1016/j.msea.2017.10.074.
- [9] Z.Y. Liang, X. Wang, W. Huang, M.X. Huang, Strain rate sensitivity and evolution of dislocations and twins in a twinning-induced plasticity steel, *Acta Mater.* (2015). doi:10.1016/j.actamat.2015.01.013.
- [10] B.C. De Cooman, Y. Estrin, S.K. Kim, Twinning-induced plasticity (TWIP) steels, *Acta Mater.* (2018). doi:10.1016/j.actamat.2017.06.046.
- [11] M. Koyama, T. Sawaguchi, K. Tsuzaki, Deformation Twinning Behavior of Twinning-induced Plasticity Steels with Different Carbon Concentrations – Part 2: Proposal of Dynamic-strain-aging-assisted Deformation Twinning, *ISIJ Int.* (2015). doi:10.2355/isijinternational.isijint-2015-070.
- [12] S.J. Lee, J. Kim, S.N. Kane, B.C. De Cooman, On the origin of dynamic strain aging in twinning-induced plasticity steels, *Acta Mater.* (2011). doi:10.1016/j.actamat.2011.07.040.
- [13] S.K. Oh, M.E. Kilic, J.B. Seol, J.S. Hong, A. Soon, Y.K. Lee, The mechanism of dynamic strain aging for type A serrations in tensile flow curves of Fe-18Mn-0.55C (wt.%) twinning-induced plasticity steel, *Acta Mater.* (2020).

- doi:10.1016/j.actamat.2020.02.020.
- [14] S. Hwang, M. heom Park, Y. Bai, A. Shibata, W. Mao, H. Adachi, M. Sato, N. Tsuji, Mesoscopic nature of serration behavior in high-Mn austenitic steel, *Acta Mater.* 205 (2021) 116543. doi:10.1016/j.actamat.2020.116543.
- [15] A. Roth, T.A. Lebedkina, M.A. Lebyodkin, On the critical strain for the onset of plastic instability in an austenitic FeMnC steel, *Mater. Sci. Eng. A.* 539 (2012) 280–284. doi:https://doi.org/10.1016/j.msea.2012.01.094.
- [16] P.D. Zavattieri, V. Savic, L.G. Hector, J.R. Fekete, W. Tong, Y. Xuan, Spatio-temporal characteristics of the Portevin–Le Châtelier effect in austenitic steel with twinning induced plasticity, *Int. J. Plast.* 25 (2009) 2298–2330. doi:https://doi.org/10.1016/j.ijplas.2009.02.008.
- [17] L.P. Kubin, Y. Estrin, The portevin-Le Chatelier effect in deformation with constant stress rate, *Acta Metall.* 33 (1985) 397–407. doi:https://doi.org/10.1016/0001-6160(85)90082-3.
- [18] Y.Z. Tian, Y. Bai, M.C. Chen, A. Shibata, D. Terada, N. Tsuji, Enhanced Strength and Ductility in an Ultrafine-Grained Fe-22Mn-0.6C Austenitic Steel Having Fully Recrystallized Structure, *Metall. Mater. Trans. A Phys. Metall. Mater. Sci.* 45 (2014) 5300–5304. doi:10.1007/s11661-014-2552-2.
- [19] Y.Z. Tian, Y. Bai, L.J. Zhao, S. Gao, H.K. Yang, A. Shibata, Z.F. Zhang, N. Tsuji, A

- novel ultrafine-grained Fe–22Mn–0.6C TWIP steel with superior strength and ductility,  
Mater. Charact. 126 (2017) 74–80. doi:10.1016/j.matchar.2016.12.026.
- [20] G.K. Williamson, W.H. Hall, X-Ray broadening from filed aluminium and tungsten,  
Acta Metall. (1953).
- [21] M.S. Paterson, X-Ray Diffraction by Face-Centered Cubic Crystals with Deformation  
Faults, J. Appl. Phys. 23 (1952) 805–811. doi:10.1063/1.1702312.
- [22] L. Balogh, G. Ribárik, T. Ungár, Stacking faults and twin boundaries in fcc crystals  
determined by x-ray diffraction profile analysis, J. Appl. Phys. (2006).  
doi:10.1063/1.2216195.
- [23] Y. Bai, H. Kitamura, S. Gao, Y. Tian, N. Park, M. Park, H. Adachi, A. Shibata, M. Sato,  
M. Murayama, N. Tsuji, Unique transition of yielding mechanism and unexpected  
activation of deformation twinning in ultrafine grained Fe-31Mn-3Al-3Si alloy, Sci. Rep.  
11 (2021) 15870. doi:10.1038/s41598-021-94800-6.
- [24] Z.C. Luo, M.X. Huang, Revisit the role of deformation twins on the work-hardening  
behaviour of twinning-induced plasticity steels, Scr. Mater. (2018).  
doi:10.1016/j.scriptamat.2017.08.017.
- [25] D. Hull, D.J. Bacon, Introduction to Dislocations, 2011. doi:10.1016/C2009-0-64358-0.
- [26] L. Král, B. Million, J. Čermák, Diffusion of Carbon and Manganese in Fe-C-Mn, Defect  
Diffus. Forum. (2007). doi:10.4028/www.scientific.net/ddf.263.153.

- 1  
2 [27] R.P. Agarwala, M.C. Naik, M.S. Anand, A.R. Paul, Diffusion of carbon in stainless steels,  
3  
4  
5 J. Nucl. Mater. 36 (1970) 41–47. doi:[https://doi.org/10.1016/0022-3115\(70\)90060-7](https://doi.org/10.1016/0022-3115(70)90060-7).  
6  
7  
8  
9 [28] W.A. Curtin, D.L. Olmsted, L.G. Hector, A predictive mechanism for dynamic strain  
10  
11 ageing in aluminium–magnesium alloys, Nat. Mater. 5 (2006) 875–880.  
12  
13  
14 doi:[10.1038/nmat1765](https://doi.org/10.1038/nmat1765).  
15  
16  
17  
18 [29] H. Aboulfadl, J. Deges, P. Choi, D. Raabe, Dynamic strain aging studied at the atomic  
19  
20  
21 scale, Acta Mater. 86 (2015) 34–42. doi:<https://doi.org/10.1016/j.actamat.2014.12.028>.  
22  
23  
24  
25  
26  
27  
28  
29  
30  
31  
32  
33  
34  
35  
36  
37  
38  
39  
40  
41  
42  
43  
44  
45  
46  
47  
48  
49  
50  
51  
52  
53  
54  
55  
56  
57  
58  
59  
60  
61  
62  
63  
64  
65